J Mater Sci (2007) 42:8943–8956
DOI 10.1007/s10853-007-1649-z

Mechanics of the hysteretic large strain behavior of mussel byssus threads

Katia Bertoldi · Mary C. Boyce

Received: 21 December 2006 / Accepted: 1 March 2007 / Published online: 7 August 2007

Abstract Natural fibers are particularly interesting from a materials point of view since their morphology has been tailored to enable a wide range of macroscopic level functions and mechanical properties. In this paper, we focus on mussel byssal threads which possess a morphology specifically designed to provide a hysteretic yet resilient large strain deformation behavior. X-ray diffraction studies have shown that numerous natural fibers have a multi-domain architecture composed of folded modules which are linked together in series along a macromolecular chain. This microstructure leads to a strong rate and temperature dependent mechanical behavior and one which exhibits a stretch-induced softening of the mechanical response as a result of the underlying morphology evolving with imposed stretched. This paper addresses the development of a constitutive model for the stress–strain behavior of the distal portion of mussel byssal threads based on the underlying protein network structure and its morphology evolving with imposed stretched. The model will be shown to capture the major features of the stress–strain behavior, including the highly nonlinear stress–strain behavior, and its dependence on strain rate and stretch-induced softening.

K. Bertoldi · M. C. Boyce (✉)
Department of Mechanical Engineering, Massachusetts Institute of Technology, Room 1-304, 77 Massachusetts Avenue, Cambridge, MA 02139, USA
e-mail: mcboyce@mit.edu

K. Bertoldi
e-mail: bertoldk@mit.edu

Introduction

Mussels live in dense beds, along the surf swept rocks of the coast. Their success in aquatic habitats is based on their ability to adhere to the rocks using the mussel byssus, which typically consists of 20–60 byssal threads. Each thread (having a total length of $\simeq$ 3 mm and a diameter of $\simeq$ 0.1 mm) consists of three regions, which differ in both morphology and mechanical properties [1–4] (see detail in Fig. 1): the *adhesive plaque*, the *distal region* and the *proximal region*. The proximal region, which represents one third of the total fiber length, consists of a crimped sheath which covers loosely packed coiled fibrils, whereas the smoother and narrower distal region is formed by bundles of densely packed filaments. From a mechanical point of view, the proximal region is extremely compliant, giving a rubber-like behavior, whereas the distal region is stiffer and less extensible (see Fig. 1) exhibiting a highly hysteretic large deformation behavior. In this study we will focus on the behavior of the distal segment, developing a constitutive model for this region. The model will be shown to capture the major features of the stress–strain behavior of the byssal thread, including the highly nonlinear stress–strain behavior, and its dependence on strain rate and stretch-induced softening.

Background

Microstructure of the distal region

Transmission Electron Microscopy analysis [1–3] reveal that all parts of the byssus are formed by the same basic filamentous components (diameter 7–9 nm) organized in different ways at the submicroscopic level and embedded

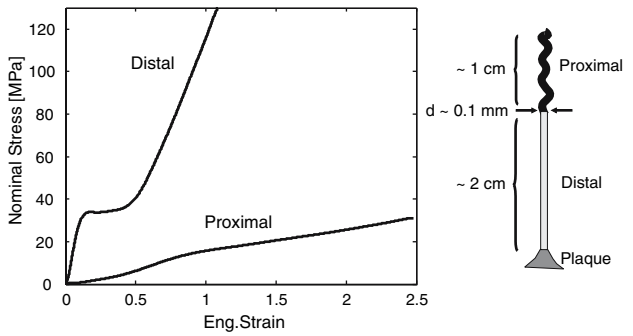

Fig. 1 Nominal stress-engineering strain behavior in uniaxial tension of the distal and the proximal region of *Mytilus californianus* at an extension rate of 10 mm/min (data replotted from Carrington and Gosline [5]). The unstressed length of the specimen is l_0 = 5.4 mm for the proximal region and l_0 = 12.5 mm for the distal region

in a microfibrillar matrix. In the proximal portion a corrugated superficial dense layer covers a central region characterized by undulating filamentous strands and individual coiled filaments embedded in an abundant and loose microfilamentous matrix. In contrast, in the distal region the outer dense layer is smooth and covers a spongy structure with tubular cavities lined by a compact tissue (Fig. 2). The tissue consists of filaments extended linearly, regularly arranged nearly parallel to the major axis of the thread and embedded in a dense matrix with a microfilamentous structure (Fig. 2a). More recently, the fiber has been found to be of a collagenous nature [6, 7]; byssal collagen has a block copolymer structure of alternating hard and soft blocks (preCOLs) consisting of a central collagen domain flanked by elastin-like or silk-like domains and terminated at both ends by histidine- and DOPA-sequences (Fig. 3a). In addition, Hassenkam et al. [8] showed that the preCOLs organize themselves into hexagonal (6 + 1) bundles that are banana-shaped (Fig. 3b). The presence of two bumps along the preCOLs has also been observed. AFM images of a stretched byssal thread suggest that the macroscopic strain is accommodated by both the elimination of the tilt seen in the unstrained thread and the unraveling of the flanking globular domains. The initial angular or 'bent' structure may act to lock the neighboring fibres and prevent intermolecular shear/sliding within the bundles.

Stress–strain behavior of the distal region

The mechanical behavior of the distal region of *Mytilus californianus* has been characterized using

- quasi-static tensile tests [4];
- cyclical loading tests [5];
- tensile test at different strain rates [5].

The mechanical tests have been performed using an Instron-1122 tensometer and a custom-made tensometer [4], capable of a maximum extension rate of 1,000 mm/min.

Interestingly, the stress–strain curve of the distal region shows the typical features of polymer response to large-strain uniaxial deformation (see Fig. 1): an initially stiff response, a clear 'yielding' point, followed by a stress plateau and subsequent strain hardening.

The 'yielding' (at approximately 15% extension) plays an important function on the thread behavior: the material response is stiff prior to yield, yield then provides the extensibility needed to distribute the load over multiple threads at relatively constant load on an individual thread. Hence, 'yield' also limits the load level transferred to the

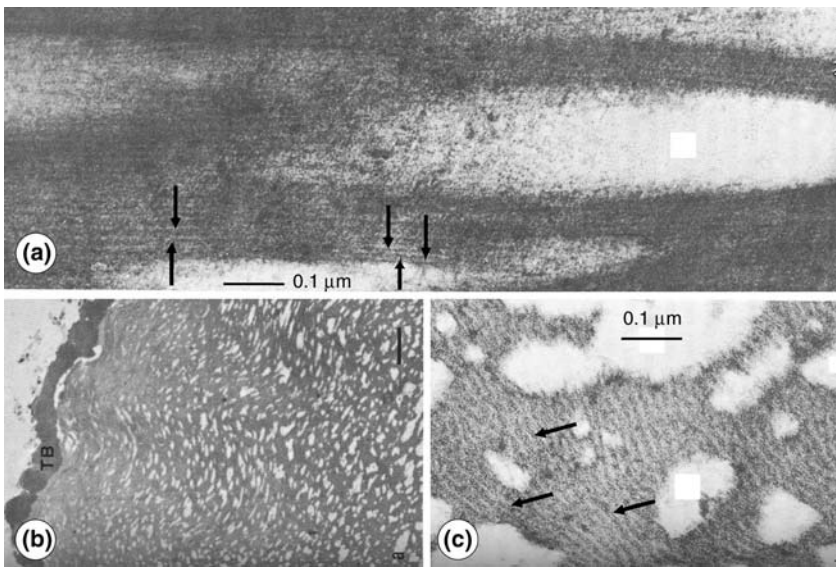

Fig. 2 Distal part of the byssus of *Mytilus galloprovincialis*. (**a**) Longitudinal section showing the filaments (arrows) running parallel to the thread axis and tubular cavities. (**b**) Cross section showing the cavities dispersed in a homogeneous tissue. (**c**) Oblique section evidencing the filaments (arrows) and their regular pattern. (From Bairati and Vitellaro-Zuccarello [1])

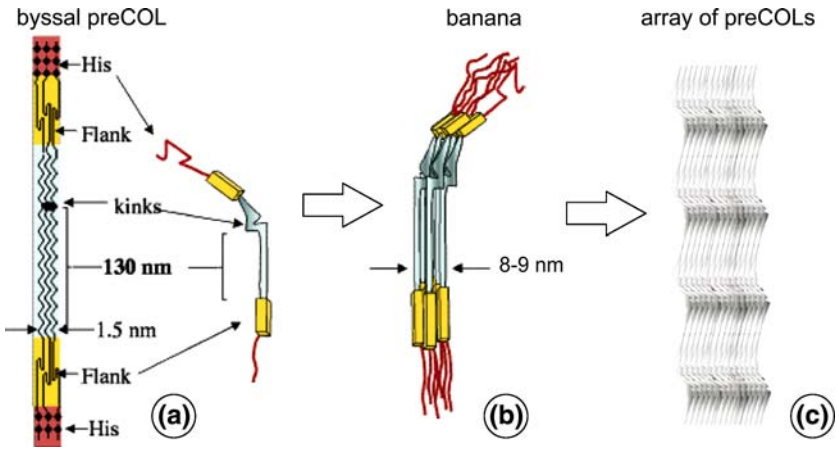

Fig. 3 (**a**) Block domain structure of byssal preCOLs (as observed in *Mytilus galloprovincialis*); (**b**) the hexagonal (6 + 1) bundles of bent-core preCOLs in the banana configuration; (**c**) Model of an array of preCOLs bundles. (From Hassenkam et al. [8])

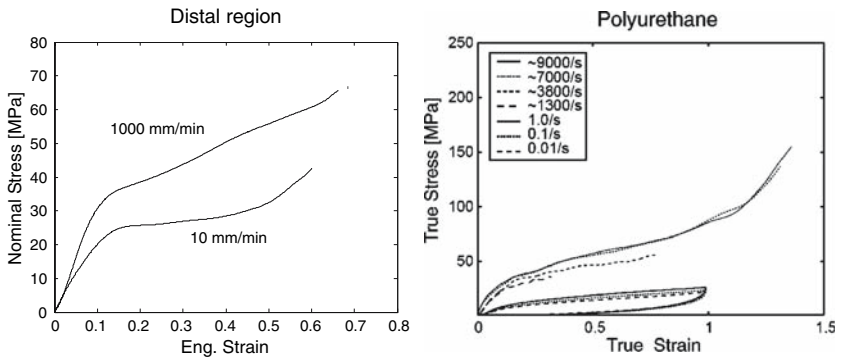

Fig. 4 Nominal stress-engineering strain behavior in uniaxial tension of the distal region of *Mytilus californianus* at extension rates of 10 mm/min and 1,000/mm (left) (data replotted from Carrington and Gosline [5]). The true stress–true strain behavior of polyurethane PU1 at quasi-static and high strain rate regimes is shown on the right (data replotted from Yi et al. [9])

adhesive plaque which helps to maintain adhesion to the surface.

Rate dependence

Samples from the distal region of byssal threads of *Mytilus californianus* have been tested in uniaxial tension at extension rates of 10 and 1,000 mm/min (see Fig. 4), corresponding to 0.0133/s and 1.33/s, respectively.[1] The higher the strain rate, the larger the stress and the yielding stress, whereas the yield strain remains relatively unchanged. In addition, at the highest strain rate, the plateau following yielding is less distinct. Again we observe that synthetic copolymers such as thermoplastic polyurethanes [9] (see detail in Fig. 4) as well as ethylene methacrylic acid [10] exhibit a microdomain or aggregated structural features and similar mechanical behavior.

[1] The unstressed length of the specimens used in the tests is not mentioned in Carrington and Gosline [5]. In the present paper, we use an initial length l_0 = 12.5 mm, value reported in Bell and Gosline [4].

Cyclical loading

Cyclic tests at different strain levels have been conducted for the distal regions of threads of *Mytilus californianus*. Figure 5 shows the nominal stress-engineering strain behavior at strain levels of 0.08 (Fig. 5a), 0.16 (Fig. 5b), 0.35 (Fig. 5c) and 0.65 (Fig. 5d). When the thread is loaded beyond its yield point, much of the energy is dissipated via deformation in the distal region. Hysteresis is a crucial property for the thread, since it reflects a shock-damping capacity: as the wave passes, the thread unloads and due to energy dissipation the creature is not dashed against the rocks.

The reloading stress–strain curves show a significantly more compliant character when compared to the initial loading behavior; this effect is known as softening behavior and it is typical of many copolymeric materials (see, for example, [9, 11]). Similar again to the copolymer behavior, the unloading paths after a given strain all follow the same curve, independent of the cycle. Both the hysteretic and softening behaviors are strain-dependent: hysteresis and softening increase with increasing strain.

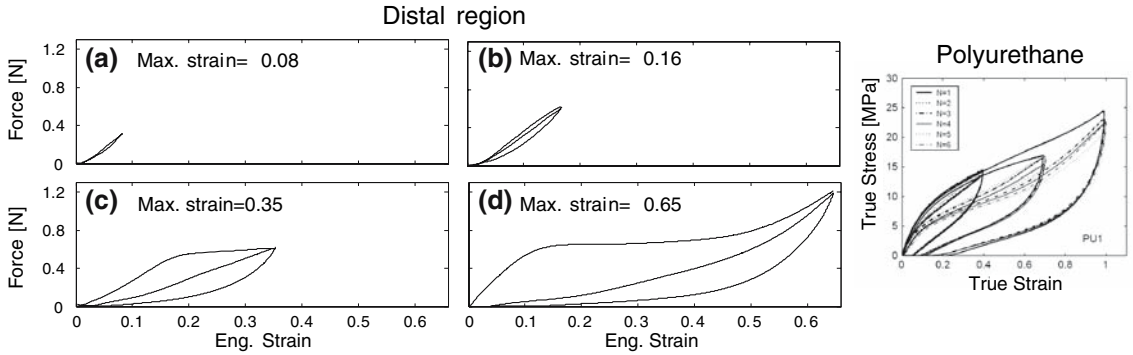

Fig. 5 Force-engineering strain behavior of distal portions of byssal threads of *Mytilus californianus* at cyclic uniaxial tests (data replotted from Carrington and Gosline [5]). Four different strain levels are considered: (**a**) 0.08 (extension rate = 5 mm/min), (**b**) 0.16 (extension rate = 5 mm/min), (**c**) 0.35 (extension rate = 10 mm/min), (**d**) 0.65 (extension rate = 10 mm/min). The true stress–true strain behavior of polyurethane PU1 at cyclic uniaxial compression tests at engineering strain rate $\dot{\epsilon} = 0.063$ /s is shown on the right (data replotted from Yi et al. [9])

In addition, after unloading, the distal region increases in stiffness with time and gradually returns to its initial structure and mechanical behavior [5] (see Fig. 6).

Micromechanical model

To understand the mechanisms that govern the behavior of the distal portion of byssal threads, a micromechanical model, representative of the underlying structure, is developed. The model framework permits us to derive the macroscopic mechanical response from the material microstructure. The development of a micromechanical model requires:

- the geometric definition of a representative volume element (RVE) which captures the main features of the material microstructure (see "The representative volume element (RVE)" section).
- the constitutive model for the stress–strain behavior of each phase. For this study, the distal portion of the byssal thread will be regarded as a two-phase composite: the constitutive model for the tissue will be presented in "Material constitutive behavior" section, whereas the fluid filling the cavities will be simply modeled as a hydrostatic incompressible fluid.
- the constitutive model of the boundaries between different phases. Pressure equilibrium is enforced across the fluid/tissue interface.
- the computation of the macroscopic mechanical behavior of the material based on the response of the RVE (see "RVE loading and macroscopic response" section).

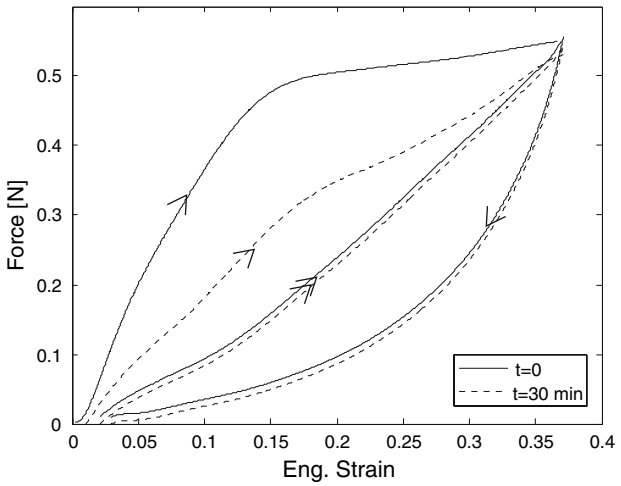

Fig. 6 Force-engineering strain behavior of distal portions of byssal threads of *Mytilus californianus* at cyclic uniaxial tests (data replotted from Carrington and Gosline [5]). Two cycles were performed at $t = 0$ (solid line), followed by two additional cycles after 30 min delay (dashed line)

The representative volume element (RVE)

As described in "Microstructure of the distal region" section, the distal region of the byssal thread consists of a spongy tissue with tubular water-filled cavities. This microstructure is idealized by a staggered array of ellipsoidal cavities (see Fig. 7).

In particular, a cylindrical cell is employed, characterized by an initial radius R_0 and initial height H_0. Following Socrate and Boyce [12], when axisymmetric loading about the z-axis is applied to the material, geometric compatibility of deformation in the two families of antisymmetric cells requires that

$$[R(\xi)]^2 + [R(H_0 - \xi)]^2 = 2[R(\xi = 0.5H_0)]^2, \quad (1)$$

where $R(z) = R_0(z) + u_r(z)$ and ξ denotes the axial coordinate for points at the outer radius of the cell in the undeformed configuration. In addition, to enforce

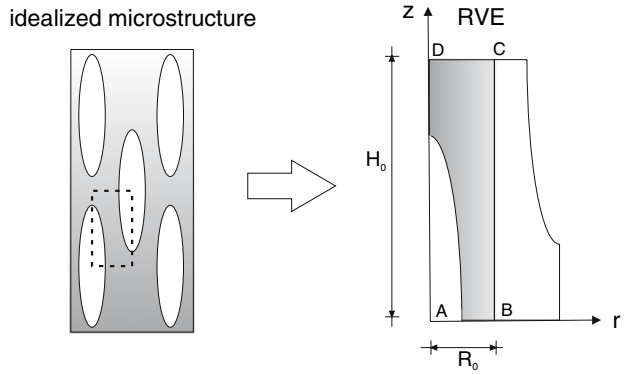

Fig. 7 Construction of the RVE (defined by the rectangle ABCD on the right) based on a staggered array of ellipsoidal fluid pockets; z is the thread axis

symmetry of the axial deformation about the cell midplan ($z = H/2$) for the two families of antisymmetric

$$u_z(\xi) + u_z(H_0 - \xi) = 2u_z(\xi = 0.5H_0). \tag{2}$$

Equations 1 and 2 define the constraints to be imposed to the RVE due to the presence of the anti-symmetric families of cells.

RVE loading and macroscopic response

When the RVE is subjected to an axial loading condition, the top edge CD moves in z-direction, $u_r\,|_{AD} = 0$, $u_z\,|_{AB} = 0$, whereas $u_r\,|_{BC}$ and $u_z\,|_{BC}$ satisfy Eqs. 1 and 2.

The macroscopic stretch in axial and hoop direction are given by

$$\overline{\lambda}_z = 1 + \frac{u_z|_{CD}}{H_0}, \quad \overline{\lambda}_\theta = 1 + \frac{u_r|_{BC}}{R_0}, \tag{3}$$

whereas, employing the average stress theorem (e.g., [13]), the macroscopic cartesian stress components $\overline{\sigma}_{ij}$ can be expressed as

$$\overline{\sigma}_{ij} = \frac{1}{V}\int_V \sigma_{ij} dV = \frac{1}{V}\int_S \sigma_{ik} n_k x_j dS, \tag{4}$$

(where x_j is the position vector and $\mathbf{n}$ the outward normal), allowing us to work in terms of tractions on the boundary.

Material constitutive behavior

The byssal thread of marine mussels is a fiber-reinforced composite material, in which a microfibrillar matrix is reinforced by stronger fibers. Following pioneering work of Spencer [14], the mechanical response of hyper-elastic fiber-reinforced materials has been investigated by Bischoff et al. [15, 16] who developed an anisotropic molecular network model for skin tissue, Holzapfel [17, 18] in a model of arterial wall tissue, Horgan and Saccomandi [19] in the developments of a model for a matrix reinforced by fibers characterized by limiting extensibility, Cantournet et al. [20] in the investigation of the effects of carbon nanotubes on the mechanical behavior of elastomeric materials.

Let $\mathbf{F} = \partial\mathbf{x}/\partial\mathbf{x}_0$ be the deformation gradient, mapping a material point from the reference position $\mathbf{x}_0$ to its current location $\mathbf{x}$ and J be its determinant, $J = \det\mathbf{F}$.

For an isotropic hyperelastic material the strain energy density W is a function of the invariants of the right Cauchy-Green tensor $\mathbf{C} = \mathbf{F}^T\mathbf{F}$ (or, alternatively, also the left Cauchy-Green tensor $\mathbf{B} = \mathbf{F}\mathbf{F}^T$),

$$W = W(I_1, I_2, I_3), \tag{5}$$

where

$$I_1 = \mathrm{tr}\mathbf{C}, \quad I_2 = \frac{1}{2}\left[(\mathrm{tr}\mathbf{C})^2 - \mathrm{tr}\mathbf{C}^2\right], \quad I_3 = \det\mathbf{C} = J^2, \tag{6}$$

I_1 being essentially a scalar equivalent stretch measure and I_3 the square of the volume ratio. For an isotropic material reinforced by a single family of fibers with direction $\mathbf{v}_0$ in the reference configuration, the strain energy density W is given by [14]

$$W = W(I_1, I_2, I_3, I_4, I_5) \tag{7}$$

where

$$I_4 = \mathbf{v}_0 \cdot \mathbf{C}\mathbf{v}_0, \quad I_5 = \mathbf{v}_0 \cdot \mathbf{C}^2\mathbf{v}_0, \tag{8}$$

I_4 being a measure of the fiber stretch. If n families of reinforcing fibers each characterized by a direction $\mathbf{v}_0^{(i)}$ are considered, Spencer [14] has shown that the strain energy density W depends not only on $I_4^{(i)}$ and $I_5^{(i)}$, but also on higher order invariants, which capture the interaction effects between different fiber families. However, the dependence of the material response on I_2, $I_5^{(i)}$ and the higher order invariants is generally weak, so that the strain energy can be simplified as

$$W = W_{\mathrm{iso}}(I_1, I_3) + W_{\mathrm{ani}}(I_4^{(i)}). \tag{9}$$

where the isotropic term W_{iso} reflects the contribution of the microfibrillar matrix and the anisotropic term W_{ani} captures the stiffening effect of the preferentially aligned fibrous network.

Microfibrillar matrix behavior

No detailed information is available on the structure of the microfibrillar matrix, and the identification of its protein content is a topic of investigation [21]. Therefore, the matrix is modeled as an isotropic, hyperelastic and mechanically nearly-incompressible Neo-Hookean material. To include compressibility a bulk strain energy term is added to the strain energy [22, 23], so that the total strain energy of the material is given by

$$W_{\text{iso}} = \frac{\mu}{2}(I_1 - 3) - \mu \log J + \frac{K}{2}(J-1)^2, \tag{10}$$

where μ and K denote the shear and bulk modulus, respectively. The first Piola-Kirchhoff stress tensor $\mathbf{S}_{\text{iso}}$ is found by differentiation with respect to $\mathbf{C}$

$$\mathbf{S} = 2\mathbf{F}\frac{\partial W}{\partial \mathbf{C}}, \tag{11}$$

yielding

$$\mathbf{S}_{\text{iso}} = \mu\mathbf{F} + [JK(J-1) - \mu]\mathbf{F}^{-T}. \tag{12}$$

The corresponding Cauchy stress, $\boldsymbol{\sigma} = \frac{1}{J}\mathbf{S}\mathbf{F}^T$, is given by

$$\boldsymbol{\sigma}_{\text{iso}} = \frac{\mu}{J}(\mathbf{B} - \mathbf{I}) + K(J-1)\mathbf{I}. \tag{13}$$

Fibrous network behavior

In this section the three-dimensional constitutive model for the highly non-linear stress–strain behavior of the fibrous network is developed. This model is based on a mathematical representation of the network structure together with a model of the axial force-displacement behavior of a single fiber.

Recently, single molecule force-extension tests showed that the behavior of many protein molecules (including muscle protein titin [24], extracellular matrix protein tenascin [25], the red blood cell cytoskeleton protein spectrin [26] and lustrin A [27]) exhibit a 'saw-tooth' profile (Fig. 8). Proteins are often characterized by a multi-domain architecture composed of folded modules which are linked together in series along the macromolecule. When a critical stress level is reached inside the folded domains, the folded modules will begin to sequentially unfold, releasing additional contour length that makes the macromolecule response more compliant and leads to a distinct drop in load.

Waite et al. [7] showed that the collagen contained in byssal threads (from both *M. edulis* and *M. galloprovincialis*) is characterized by a breaking strain that greatly exceeds the ultimate strain for more typical collagenous

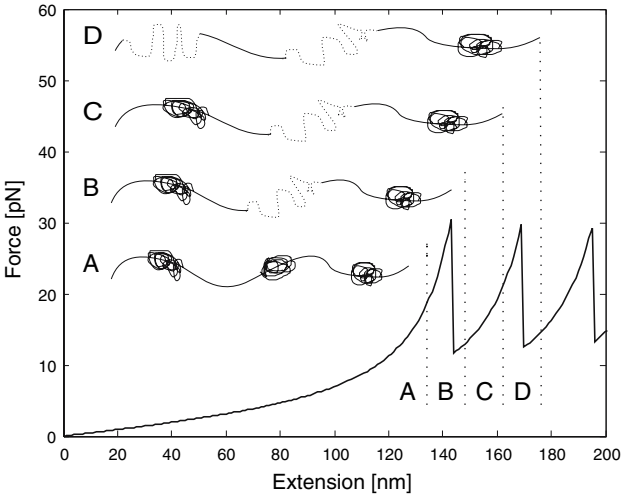

Fig. 8 Typical 'saw-tooth' profile obtained from single molecule force-extension tests of protein molecules. (**a**) The molecule is stretch until the held force is such that unfolding becomes highly probable. (**b**) Unfolding of a domain abruptly reduces the holding force, since additional contour length is released. (**c**–**d**) The molecule is stretched again until a force is reached where the next domain unfolds. (From [24])

structures, such as tendons. This large increase in length of the preCOL's structure after stretch can only be explained by the unraveling of the globular domains (Fig. 9), which is taken into account in this study.

Since the preCOLs are incorporated into a continuous three-dimensional macromolecular protein network, the unfolding process affecting its constituent fibrils generates a plateau in the stress–strain behavior. Therefore, the unfolding of the globular domain permits us to explain the nature of the 'yield' point that characterizes the stress–strain behavior of the distal segment (Fig. 1) and the resulting highly compliant and elastic unloading/reloading behavior.

Network model: The fibrous network, in a simplified mathematical representation, is described by:

- an average fiber end-to-end distance, r_0;
- an average fully extended end-to-end distance, L;

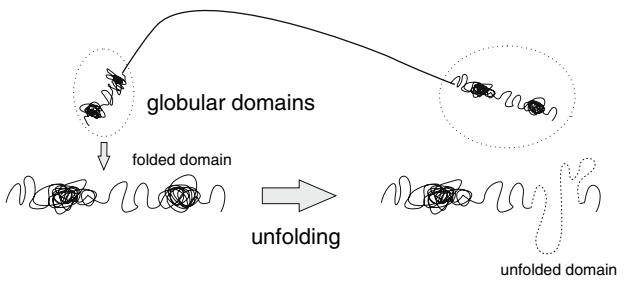

Fig. 9 Byssal preCOL flanked by globular domains that unfold when stretched

- an idealized network connectivity;
- an average initial orientation of the fibers, θ_0.

To capture the initial orthotropy of the network with a preferred fiber orientation, an eight-chain orthotropic unit cell is employed, as proposed by Bischoff et al. [15, 16]. The eight-chain network considers an idealized structure of 8 fibers located along the diagonals of a prismatic cell (with dimensions a, b and c along the material axes singled out by the unit vectors $\hat{\mathbf{e}}_a$, $\hat{\mathbf{e}}_b$ and $\hat{\mathbf{e}}_c$, respectively) (Fig. 10). However, in this study the material axes will be aligned with the coordinate axes singled out by the unit vectors $\hat{\mathbf{e}}_1$, $\hat{\mathbf{e}}_2$ and $\hat{\mathbf{e}}_3$ and we will assume $a = c$, so that the initial cell can be completely defined by the undeformed end-to-end distance r_0 and the average fiber orientation θ_0,

$$a = c = \sqrt{2} r_0 \sin\theta_0, \quad b = 2 r_0 \cos\theta_0. \tag{14}$$

Therefore, the initial direction of each fiber in the cell is described by the unit vectors

$$\begin{aligned}
\mathbf{v}_0^{(1)} &= -\mathbf{v}_0^{(5)} = v_{01}\hat{\mathbf{e}}_1 + v_{02}\hat{\mathbf{e}}_2 + v_{01}\hat{\mathbf{e}}_3,\\
\mathbf{v}_0^{(2)} &= -\mathbf{v}_0^{(6)} = v_{01}\hat{\mathbf{e}}_1 + v_{02}\hat{\mathbf{e}}_2 - v_{01}\hat{\mathbf{e}}_3,\\
\mathbf{v}_0^{(3)} &= -\mathbf{v}_0^{(7)} = v_{01}\hat{\mathbf{e}}_1 - v_{02}\hat{\mathbf{e}}_2 + v_{01}\hat{\mathbf{e}}_3,\\
\mathbf{v}_0^{(4)} &= -\mathbf{v}_0^{(8)} = v_{01}\hat{\mathbf{e}}_1 - v_{02}\hat{\mathbf{e}}_2 - v_{01}\hat{\mathbf{e}}_3,
\end{aligned} \tag{15}$$

where

$$v_{01} = \frac{1}{\sqrt{2}}\sin\theta_0, \quad v_{02} = \cos\theta_0. \tag{16}$$

The long, continuous nature of the fibers permits the assumption of affine deformation, giving the fiber stretch $\lambda_f^{(i)}$ of the i-th fiber to be

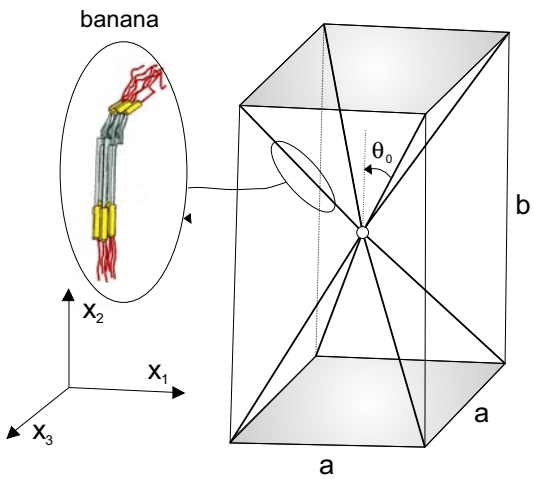

Fig. 10 Eight-chain, three-dimensional orthotropic unit cell

$$\lambda_f^{(i)} = \sqrt{\mathbf{v}_0^{(i)} \cdot \mathbf{C}\mathbf{v}_0^{(i)}} = \sqrt{I_4^{(i)}}. \tag{17}$$

Fiber strain energy: The three-dimensional stress–strain behavior of the fibrous network can be determined employing the orthotropic eight-chain network together with a representation of the axial force-stretch behavior of a bent protein fiber containing folded domains. In determining the axial force-stretch behavior of such fibers, we need to derive an expression for the force–displacement relation when axially stretching the fiber by displacing the two end points and thus increasing the end-to-end distance from r_0 to r. The fiber stretching is thus given by $\lambda_f = r/r_0$ and may be multiplicatively decomposed into unbending and axial stretching components following a Kroner–Lee decomposition [28, 29] (Fig. 11),

$$\lambda_f = \lambda_f^s \lambda_f^u, \tag{18}$$

where λ_f^u and λ_f^s denote the stretch accommodated by unbending and stretching, respectively. The force-stretch behavior will consist of an initially compliant region where the axial stretch is primarily accommodated by the unbending of the fiber; as the fiber straightens, the force-stretch behavior stiffens, since the fiber will now be directly axially stretched.

Idealizing the bent fiber to consist of two long, straight, stiff segments of length L_1 and L_2 joined by a bend as shown in Fig. 12, an expression for the fiber strain energy contribution due to unbending is obtained (see Appendix A)

$$w_f^u = \frac{EI}{2\rho_0\alpha_0}(\alpha - \alpha_0)^2 \tag{19}$$

where EI is the bending stiffness of the fiber, ρ_0 the initial bend radius and $\alpha_0 = \alpha_{10} + \alpha_{20}$ and $\alpha = \alpha_1 + \alpha_2$ the initial and current bend angle, respectively, given by

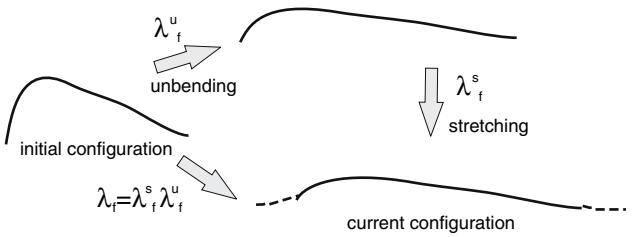

Fig. 11 Schematic of decomposition of λ_f into unbending and stretching parts

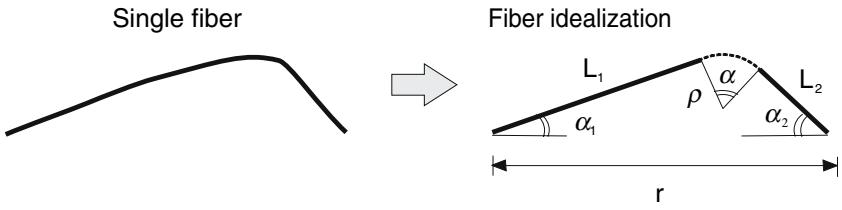

Fig. 12 Single bent fiber (left) and its approximation into two rigid segments of length L_1 and L_2 connected by a circular bend

$$\alpha_1 = \arcsin\left[\frac{\sqrt{4L_2^2(\lambda_f^u)^2r_0^2-\left[(\lambda_f^u)^2r_0^2+L_2^2-L_1^2\right]^2}}{2\lambda_f^u r_0 L_1}\right],$$
$$\alpha_2 = \arccos\left[\frac{(\lambda_f^u)^2r_0^2+L_2^2-L_1^2}{2\lambda_f^u r_0 L_2}\right]. \tag{20}$$

Models treating the chain as an entropic wormlike chain (WLC) and incorporating additional stretching terms appropriate for enthalpic contributions have been developed for polymers [30, 31]. However, here, the increase of the fiber contour length during unfolding is taken to be gradual and slow, so that its thermal fluctuations may be neglected. Thus, the fiber strain energy contribution due to axial stretching is simply taken as

$$w_f^s(\lambda_s) = \frac{EA}{2L}r_0^2(\lambda_f^s-1)^2, \tag{21}$$

where EA denotes the fiber axial stiffness and L the fiber contour length. The axial force versus extension relationship is obtained via $f = \frac{\partial w}{\partial r}$, yielding

$$f^u = \frac{2EI}{\alpha_0\rho_0}\frac{\lambda_f^u r_0(\alpha-\alpha_0)}{\sqrt{4L_2^2(\lambda_f^u)^2r_0^2-\left[(\lambda_f^u)^2r_0^2+L_2^2-L_1^2\right]^2}}, \tag{22}$$

and

$$f^s = \frac{EA}{L}r_0(\lambda_f^s-1), \tag{23}$$

and fiber equilibrium requires that

$$f = f^u = f^s. \tag{24}$$

Therefore, employing Eqs. 18 and 22–24, λ_f^u and λ_f^s can be solved.

Unfolding criterion: The unfolding is a thermally activated process whereby stress on the folded domains lowers the energy barrier of unfolding and hence increases its probability. It is introduced to the fibrous network by specifying the evolution of the contour length of its constituents. Here, following Qi et al. [32], the rate dependence of unfolding is captured by an Eyring model [33, 34]

$$\dot{L}_u = \alpha_u(L_{\max}-L_t)\exp\left[\frac{f_c x_u}{k_B T}\right], \tag{25}$$

where

$$\alpha_u = \dot{L}_{0u}\exp\left[-\frac{\Delta G_u}{k_B T}\right] \tag{26}$$

is a lumped parameter. In Eqs. 25 and 26 $\dot{L}_{0u}$ denoted the pre-exponential factor, ΔG_u the energy barrier to unfolding, x_u the width of the activation barrier, L_t the current fibril contour length, $L_{\max}$ the maximum fibril contour length, T the absolute temperature and k_B the Boltzmann constant. Therefore, the fiber contour length is updated as

$$L_{t+\Delta t} = L_t + \dot{L}_u\Delta t. \tag{27}$$

The limited stress–strain data available at different rates makes it difficult to more fully assess the approximation of an Eyring model; more data is needed to either confirm this approach or to point to other process models.

Note that refolding is an extremely low probability during stretching and thus is neglected. This will be discussed later.

Fibrous network stress–strain behavior: The strain energy density of the fibrous network is determined using both the expression for the fibril strain energy and the orthotropic eight-chain network structure.

When the cell is stretched, its strain energy is simply given by the sum of the strain energy of the eight constituent fibers

$$W_{\text{cell}} = 2\sum_{i=1}^{4} w(\lambda_f^{(i)}), \tag{28}$$

(the fact that the stretch of fibers $\mathbf{v}_0^{(1-4)}$ is the same as in fibers $\mathbf{v}_0^{(5-8)}$ has been used), so that the strain energy density is given by

$$W_{\text{ani}} = \frac{W_{\text{cell}}}{abc} = \frac{v}{4}\sum_{i=1}^{4} w(\lambda_f^{(i)}), \tag{29}$$

where v denotes the fiber density (number of fibers per unit reference volume). At this point, the first Piola-Kirchhoff

stress tensor $\mathbf{S}_{\text{ani}}$ can be obtained by differentiation of the strain energy density

$$\mathbf{S}_{\text{ani}} = 2\mathbf{F}\frac{\partial W_{\text{ani}}}{\partial \mathbf{C}} = 2\mathbf{F}\left(\frac{v}{4}\sum_{i=1}^{4}\frac{\partial w_f}{\partial I_4^{(i)}}\frac{\partial I_4^{(i)}}{\partial \mathbf{C}}\right), \tag{30}$$

and since $\frac{\partial I_4^{(i)}}{\partial \mathbf{C}} = \mathbf{v}_0^{(i)} \otimes \mathbf{v}_0^{(i)}$, Eq. 30 can be rewritten as

$$\mathbf{S}_{\text{ani}} = \frac{v}{4}\sum_{i=1}^{4}\frac{1}{\lambda_f^{(i)}}\frac{\partial w_f}{\partial \lambda_f^{(i)}}\mathbf{v}^{(i)} \otimes \mathbf{v}_0^{(i)}, \tag{31}$$

where $\mathbf{v}^{(i)} = \mathbf{F}\mathbf{v}_0^{(i)}$ and $\frac{\partial w_f}{\partial \lambda_f^{(i)}} = f\, r_0$. Substitution of Eqs. 23 into Eq. 31 yields

$$\mathbf{S}_{\text{ani}} = \frac{v}{4}\sum_{i=1}^{4}\frac{1}{\lambda_f^{(i)}}\left[\frac{EA}{L}r_0^2(\lambda_f^{s(i)} - 1)\right]\mathbf{v}^{(i)} \otimes \mathbf{v}_0^{(i)}, \tag{32}$$

or alternatively (substituting Eqs. 22 into 31)

$$\mathbf{S}_{\text{ani}} = \frac{v}{4}\sum_{i=1}^{4}\frac{1}{\lambda_f^{(i)}} \left[\frac{2EI}{\alpha_0\rho_0}\frac{\lambda_f^u r_0^2(\alpha - \alpha_0)}{\sqrt{4L_2^2(\lambda_f^u)^2 r_0^2 - \left[(\lambda_f^u)^2 r_0^2 + L_2^2 - L_1^2\right]^2}}\right]\mathbf{v}^{(i)} \otimes \mathbf{v}_0^{(i)}. \tag{33}$$

The corresponding Cauchy stress is given by

$$\boldsymbol{\sigma}_{\text{ani}} = \frac{v}{4J}\sum_{i=1}^{4}\frac{1}{\lambda_f^{(i)}}\left[\frac{EA}{L}r_0^2(\lambda_f^{s(i)} - 1)\right]\mathbf{v}^{(i)} \otimes \mathbf{v}^{(i)}. \tag{34}$$

Composite constitutive model

As outlined in "Material constitutive behavior" section, the strain energy function and Cauchy stress for the composite material are simply given by the sum of the matrix and fiber contributions, yielding

$$\begin{aligned}\boldsymbol{\sigma} &= \boldsymbol{\sigma}_{\text{iso}} + \boldsymbol{\sigma}_{\text{ani}} \\ &= \frac{\mu}{J}(\mathbf{B} - \mathbf{I}) + K(J-1)\mathbf{I} + \frac{v}{4J}\sum_{i=1}^{4}\frac{1}{\lambda_f^{(i)}}\left[\frac{EA}{L}r_0^2(\lambda_f^{s(i)} - 1)\right]\mathbf{v}^{(i)} \otimes \mathbf{v}^{(i)}.\end{aligned} \tag{35}$$

Model implementation

The constitutive model outlined above has been implemented into the commercial finite element code ABAQUS/Standard, Version 6.6-1, using the user subroutine UMAT. The application of this subroutine requires 10 material constants

- Isotropic matrix

μ	Initial shear modulus
K	Bulk modulus

(36)

- Fiber network

θ_0	Initial fiber orientation
E	Fiber Young's modulus
L_{10}	Initial length of one of the two stiff fiber segments
L_{20}	Initial length of the other stiff fiber segment
H_0	Initial fiber center-to-center distance
d	Fiber diameter

(37)

Therefore, the bending and axial fiber stiffnesses are given by

$$EI = E\frac{\pi d^4}{256}, \quad EA = E\frac{\pi d^2}{4}, \tag{38}$$

and the initial end-to-end distance is

$$r_0 = \sqrt{H_0^2 + L_{10}^2} + \sqrt{H_0^2 + L_{20}^2}. \tag{39}$$

- Unfolding

$L_{\max}$	Maximum fiber contour length
α_u	Lumped parameter
x_u	Width of the activation barrier

(40)

The microstructural geometry parameters have all been characterized by microscopy and documented in the literature; the remaining parameters are obtained by fitting to available mechanical stress–strain data. The values of the material constants used in the simulations presented in "Results" section are listed in Table 1. Appendix B details the procedure for obtaining these

Table 1 Material parameters used in "Results" section

μ [MPa]	7.5	K [MPa]	372.5	θ_0	25°
E [GPa]	45	L_{10} [nm]	200	L_{20} [nm]	100
H_0 [nm]	22	d [nm]	9	$L_{\max}$[nm]	385
α_u [s^{-1}]	$2.5\cdot 10^{-4}$	x_u [nm]	$1\cdot 10^{-7}$		

parameters and also describes additional tests that are needed to better facilitate the identification of these material parameters.

Results

Constitutive model

In this section, the response of the constitutive model for the distal tissue described in "Material constitutive behavior" section is investigated.

Uniaxial tension

Figure 13 demonstrates the ability of the constitutive model to capture the characteristic features of material response to large uniaxial tensile deformations: initial linear response, 'yielding', stretch-induced softening and strain hardening. The evolution of the contour length is also reported in the plot, showing the link between the material response and the unfolding process. The transition from the initially stiff to a very compliant response is due to the start of the unfolding process, whereas strain hardening begins when the unfolding process terminates. Figure 13 also shows an initially (at strain levels lower than 0.01) compliant response generated by the unbending of the banana shaped protein fiber; as the fiber straightens and it is stretched directly, the response becomes much stiffer. Finally, it is important to note that the model also captures the rate dependence of the unfolding process.

Simple shear

Figure 14 shows the material behavior for the case of simple shear loading, where

$$\mathbf{X} = \mathbf{X}_0 + \tan\,\gamma\, x_{02}\,\hat{\mathbf{e}}_1, \tag{41}$$

where γ denotes the shear angle. In this case four fibers of the eight-fiber network are observed to extend (denoted with 'Fiber A' in Fig. 14) and four are observed to compress (denoted with 'Fiber B' in Fig. 14), where the four compressed fibers begin to elongate at the largest strains since they have also rotated. When a fiber is compressed, the unfolding process is not activated and therefore the rate dependent aspect of the response of that fiber is not activated. All fibers are observed to rotate towards the shear direction further demonstrating how macroscopic deformation is accommodated by both rotation and extension/compression of the fibers.

In the case of simple shear, it is not just the azimuthal orientation (i.e., the azimuth angle with respect to the fiber axis given by the angle θ_0 in Fig. 15—left) of the fiber that

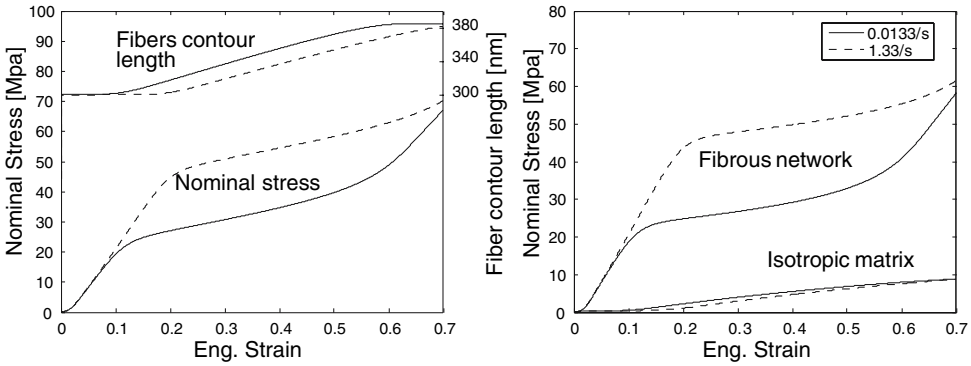

Fig. 13 Model prediction of nominal stress-engineering strain behavior in uniaxial tension for the composite material (left) together with the evolution of the fibers contour length (right axis). The separated contribution of the fibrous network and of the isotropic matrix are reported in the plot on the right

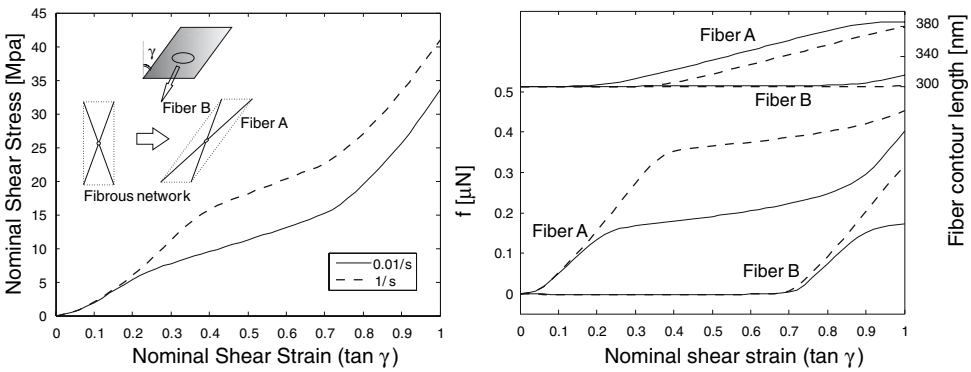

Fig. 14 Model prediction of nominal shear stress-nominal shear strain tan γ in simple shear for the composite material at shear strain rates of 0.01/s and 1/s (left). On the right, the corresponding evolution of the axial force and the contour length for both the fibers in tension and compression in the eight-chain network are reported

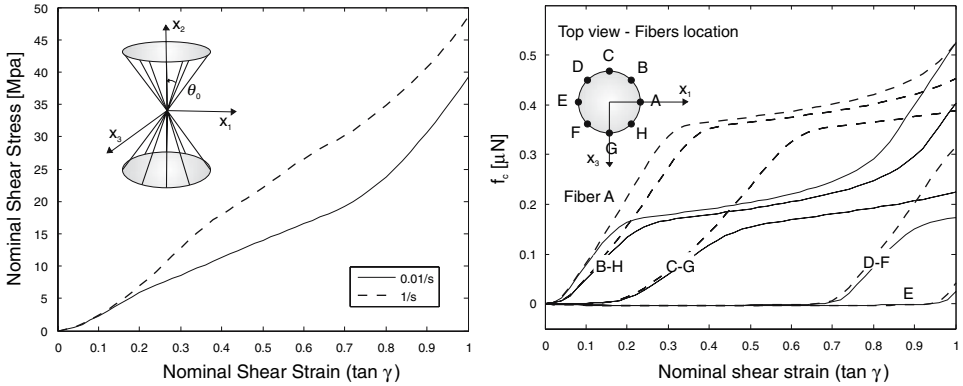

Fig. 15 Model prediction of nominal shear stress-nominal shear strain tan γ in simple shear for the composite material at shear strain rates of 0.01/s and 1/s in the case of a 16-chain network (left). On the right, the corresponding evolution of the axial force for all the fibers in the 16-chain network is reported

determines its stretch. Therefore, in addition to an eight-chain arrangement of fibers with initial azimuthal orientation of 25°, a case considering a cone of 16 fibers oriented at the azimuthal angle of 25° with the same overall fiber density is also subjected to simple shear. Figure 15 shows the material behavior for this case of 16-fiber cone oriented at $\theta_0 = 25^\circ$ and the fibers equally spaced around the cone (see detail in Fig. 15). In the uniaxial tension case the material response obtained employing the 16-chain network is exactly the same as the one obtained employing the eight-chain network. In contrast, when simple shear loading is considered, the responses given by the two different networks is slightly different, since the constituents fibers are loaded differently (Fig. 15—right).

Micromechanical model

A two-dimensional axisymmetric finite element model of the RVE of the distal segment of the thread has been constructed in the commercial code ABAQUS with a mesh constructed of 4-node, bilinear, hybrid, axisymmetric elements (CAX4H). The fluid-filled cavity has been modeled employing hydrostatic fluid elements (FAX2) and the fluid has been assumed to be incompressible with a density of $\rho = 1{,}000$ kg/m^3.

Figure 16 shows the simulation (for both the constitutive and the micromechanical model) and experimental results for uniaxial tension at a strain rate of 0.0133/s and 1.33/s. The simulations results agree very well with the experimental data and correctly capture the rate dependent behavior of the stress–strain behavior. Using the micrograph of Fig. 2 as a guide, the cavity is taken to be ellipsoidal with major and minor semi-axes a and b equal to 425 and 75 nm, respectively (see detail in Fig. 16), whereas the dimensions of the RVE are taken as 575 and 150 nm, so that the volume fraction of cavities f is equal to 0.12. In the left part of Fig. 16 the cavities are taken to be water filled, whereas the right part of Fig. 16 shows the material behavior comparing the cases when taking the cavities to be empty versus water-filled.

For the case of uniaxial tension, the water-filled and empty cavities representations yield very similar stress–strain behavior for the thread. This nearly identical behavior is a result of the cavity not providing any shear stiffness (whether water filled or empty), for this case of uniaxial tension, noting that uniaxial tension primarily samples the shear stiffness of a material for materials possessing a low shear modulus relative to the bulk modulus. In contrast, in the case of a hydrostatic loading situation, the two cases would give very different results, since we would be sampling the volumetric stiffness of the thread.

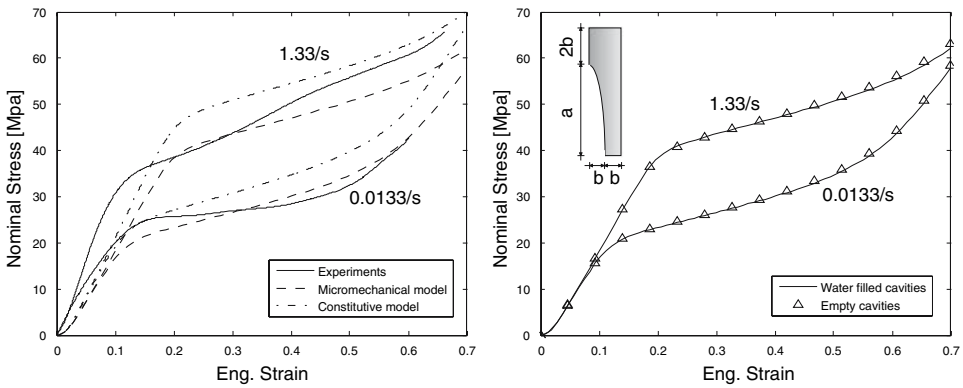

Fig. 16 Nominal stress versus engineering strain for uniaxial tension at $\dot{\epsilon} = 0.0133$ /s and $\dot{\epsilon} = 1.33$ /s. Experimental and simulation results (for both constitutive and micromechanical model with water filled cavities) are reported (left), whereas micromechanical model results obtained with empty cavities and water-filled cavities are shown on the right

In Figs. 17 and 18, the contours of the axial stress and axial strain, respectively, are plotted in the RVE for both $\dot{\epsilon} = 0.0133$ /s and $\dot{\epsilon} = 1.33$ /s at strain level equal to 0.2, 0.4 and 0.6.

Simulations on cyclic loading-unloading tests were conducted at a strain rate $\dot{\epsilon} = 0.0133$ /s and $\dot{\epsilon} = 1.33$ /s and Fig. 19 shows cyclic loading to different maximum strains. The unloading-reloading behavior shown in Fig. 19 provides the key that the 'yield' is not a classic plasticity type of yield, but it is a structural breakdown that changes the hyperelastic behavior due to unfolding.

Conclusions

A constitutive model for the hysteretic large strain behavior of the distal portion of mussel byssus threads has been presented, providing new insight into its rate dependent behavior. The constitutive model results demonstrate that the 'yielding' and the following plateau region in the stress–strain curve correspond to simultaneous fiber stretching and module unfolding taking place in the different constituents fibers. The rate effects on the stress–strain behavior due to the rate-dependence of unfolding are

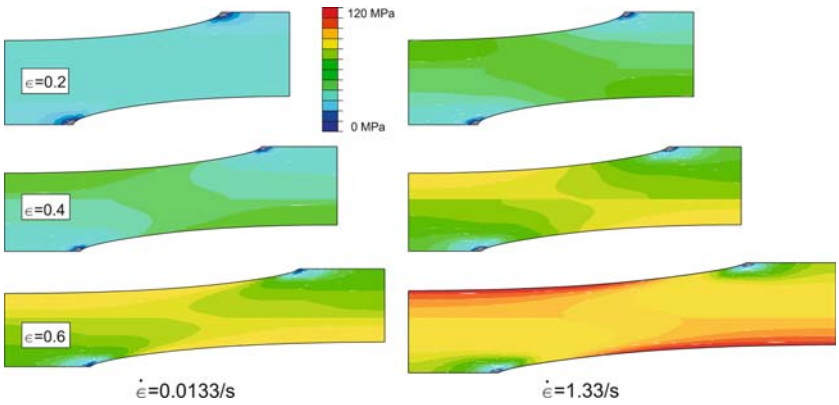

Fig. 17 Progression of axial stress during a test for the RVE with water-filled cavities loaded in uniaxial tension at $\dot{\epsilon} = 0.0133$ /s (left) and $\dot{\epsilon} = 1.33$ /s (right)

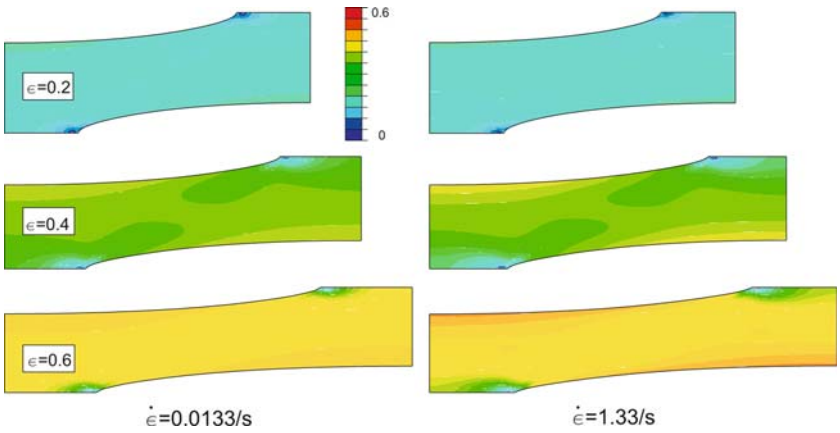

Fig. 18 Progression of axial strain during a test for the RVE with water-filled cavities loaded in uniaxial tension at $\dot{\epsilon} = 0.0133$ /s (left) and $\dot{\epsilon} = 1.33$ /s (right)

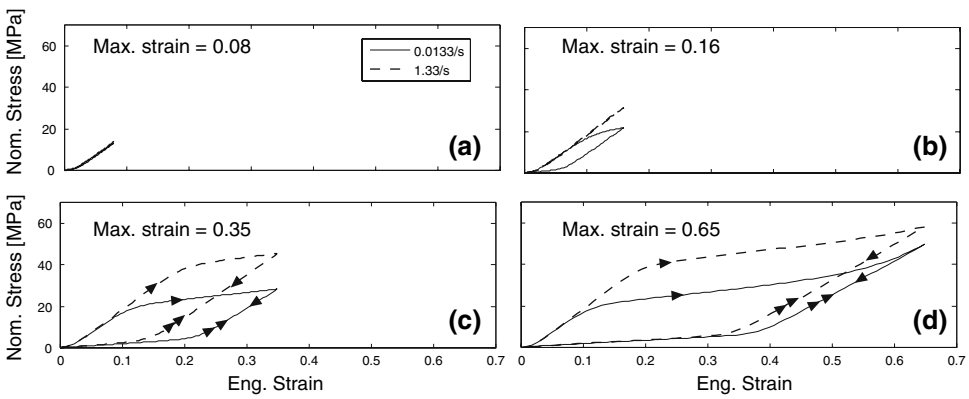

Fig. 19 Numerical simulations of cyclic (load–unload–reload) tests: Nominal stress-engineering strain behavior at at a strain rate $\dot{\epsilon} = 0.0133$ /s and $\dot{\epsilon} = 1.33$ /s. Four different strain levels are considered: (**a**) 0.08, (**b**) 0.16, (**c**) 0.35, (**d**) 0.65

also captured by the model. However the model does not capture the difference between the unloading and reloading path seen in the cyclic tests. During unloading the unfolded domains partially refolds, giving a reloading path somewhat stiffer than the unloading path (depending on the hold time between unloading and reloading). This important aspect of material behavior shall be incorporated into future extensions of the model. The model shall also be extended to the proximal region and adhesive plaque, so that it will be possible to use model-based FEM simulations to systematically investigate the behavior of multiple threads connected to the animal and their load sharing mechanisms, which will ultimately provide insights into the adhesive mechanisms of this biologically engineered system.

Finally, we would like to remark the fact that the proposed constitutive model for mussel byssus threads is a starting point to understand the role of modular protein in many biological materials, including muscles [35, 36], red blood cell membranes [37, 38] (M Arslan submitted), spider silk [39] and organic matrix in nacre [27, 40].

Acknowledgments This research was supported by the Dupont—MIT Alliance.

Appendix A: Derivation of the strain energy contribution due to unbending

Approximating the bent fiber to consist of two straight segments of length L_1 and L_2 connected by a circular bend of length $\rho\ \alpha$ (with $\alpha = \alpha_1 + \alpha_2$), as shown in Fig. 12, a form for the force-stretch behavior of the unbending of a single fiber is derived. Both segments are assumed to be rigid, so that all the deformation is accommodated by unbending of the kinked region. In addition, the contour length of the kink is assumed to be fixed (i.e. stretching of the kink region is neglected), so that

$$\rho\alpha = \rho_0\alpha_0. \tag{A.1}$$

Figure 12 clearly shows that the angles α_1 and α_2 satisfy the condition

$$L_1 \sin\alpha_1 = L_2 \sin\alpha_2, \tag{A.2}$$

and, taking $L > > \rho\ \alpha$, the fiber stretching $\lambda = r/r_0$ may be approximated as

$$\lambda = \frac{L_1\cos\alpha_1 + L_2\cos\alpha_2}{r_0}, \tag{A.3}$$

so that from Eqs. A.2 and A.3 α_1 and α_2 may be expressed as a function of λ as

$$\begin{aligned}\alpha_1 &= \arcsin\left[\frac{\sqrt{4L_2^2\lambda^2 r_0^2 - \left(\lambda^2 r_0^2 + L_2^2 - L_1^2\right)^2}}{2\lambda r_0 L_1}\right],\\ \alpha_2 &= \arccos\left[\frac{\lambda^2 r_0^2 + L_2^2 - L_1^2}{2\lambda r_0 L_2}\right].\end{aligned} \tag{A.4}$$

The strain energy of the fiber due to the unbending of the bend is given by

$$w^u = \frac{1}{2}EI(\Delta\kappa)^2\rho_0\alpha_0, \tag{A.5}$$

where EI is the bending stiffness and $\Delta\kappa$ denotes the change in curvature of the bend

$$\Delta\kappa = \left(\frac{1}{\rho} - \frac{1}{\rho_0}\right) = \frac{\alpha - \alpha_0}{\rho_0\alpha_0}. \tag{A.6}$$

Substitution of Eq. A.6 into Eq. A.5 yields

$$w^u = \frac{EI}{2\rho_0\alpha_0}(\alpha - \alpha_0)^2, \tag{A.7}$$

so that the fiber force-stretch behavior is given by

$$f^u = \frac{\partial w^u}{\partial r} = \frac{2EI}{\alpha_0\rho_0}\frac{\lambda r_0(\alpha - \alpha_0)}{\sqrt{4L_2^2\lambda^2 r_0^2 - \left(\lambda^2 r_0^2 + L_2^2 - L_1^2\right)^2}}. \tag{A.8}$$

Note that in case of a symmetrically bent fiber (i.e. $L_1 = L_2$), Eq. A.8 reduces to

$$f^u = \frac{2EI}{\alpha_0\rho_0 r_0}\frac{\alpha_0 - 2\arccos\left(\lambda\cos\frac{\alpha_0}{2}\right)}{\sqrt{1 - \left(\lambda\cos\frac{\alpha_0}{2}\right)^2}}\cos\frac{\alpha_0}{2}. \tag{A.9}$$

Appendix B: Parameter identification for the constitutive model

The mussel byssus is a biological material and thus its mechanical properties are observed to vary, mostly influenced by the season, the temperature, the water salinity [41, 42]. Thus the identification of material parameters entering in the constitutive model is aleatoric and related to all these effects. However, Figs. 1 and 4 clearly show that the stress–strain behavior of the distal segment consists of three different regions (Fig. 20):

- an initial linear response: it is used to identify the value of the fiber Young's modulus E;
- 'yielding' followed by stretch-induced softening: the 'yielding' points at different strain rates are used to identify the unfolding parameters x_u and α_u;

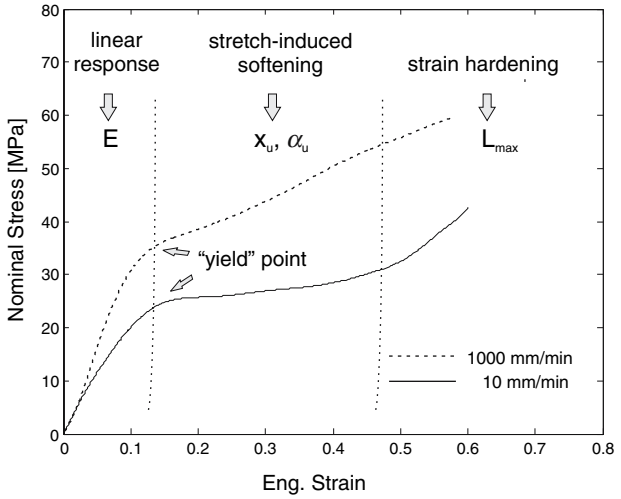

Fig. 20 Nominal stress-engineering strain behavior in uniaxial tension of the distal region at extension rates of 10 mm/min and 1,000/mm. It consists of three different regions which used to identify the material parameters

- strain hardening: it permits us to identity the length of the fully unfolded fiber L_{max}.

The geometrical parameters θ_0, L_{10}, L_{20}, H_0 and d have all been be measured with transmission electron microscopy and the values reported in Hassenkam et al. [8] are used.

To better facilitate the identification of the material parameters entering in the constitutive model additional tests are needed:

- additional tensile tests at multiple strain rates to better understand the rate-dependence of 'yield';
- Relaxation tests to better understand the sources of the rate-dependence;
- Unloading–reloading tests at higher strain rates to better understand the unloading/reloading process;
- Force test of a single macromolecule to validate the choice of material parameters.

References

1. Bairati A, Vitellaro-Zuccarello L (1976) Cell Tiss Res 166:219
2. Benedict CV, Waite JH (1986) J Morphol 189:261
3. Bairati A (1991) In: Lanzavecchia G, Valvassori R (eds) Form and function in zoology. Mucchi, Modena, pp 163–177
4. Bell E, Gosline JM (1996) J Exp Biol 199:1005
5. Carrington E, Gosline JM (2004) Am Malacol Bull 18:135
6. Coyne KJ, Qin XX, Waite JH (1997) Science 277:1830
7. Waite JH, Qin XX, Coyne KJ (1998) Matrix Biol 17:93
8. Hassenkam T, Gutsmann T, Hansma P, Sagert J, Waite JH (2004) Biomacromolecules 5:1351
9. Yi J, Boyce MC, Lee GF, Balizer E (2006) Polymer 47:319
10. Deschanel S, Boyce MC, Cohen RE (2007) Rate dependent mechanical performance of Ethylene Methacrylic Acid (EMAA) copolymers and POSS-enhanced EMAA nanocomposites. Proceedings of ACS Spring Meeting—Symposyum on segmental block copolymers, Chicago
11. Qi HJ, Boyce MC (2005) Mech Mater 37:817
12. Socrate S, Boyce MC (2000) J Mech Phys Solids 48:233
13. Gurtin ME (1972) In: Flugge S (ed) Handbuch der Physik, vol 6a(2). Springer, Berlin
14. Spencer AJM (ed) (1984) In: Continuum theory of the mechanics of fibre-reinforced composites. Springer-Verlag, New-York, pp 1–32
15. Bischoff JE, Arruda EM, Grosh K (2002) J Appl Mech 69:570
16. Bischoff JE, Arruda EM, Grosh K (2002) J Appl Mech 69:198
17. Holzapfel GA (2000) Nonlinear solid mechanics, a continuum approach for engineering. John Wiley and Sons, Chichester
18. Holzapfel GA (2003) In: Holzapfel GA, Ogden RW (eds) Biomechanics of soft tissue in cardiovascular systems CISM lectures, vol 441. Springer, Wien, pp 109–184
19. Horgan CO, Saccomandi G (2005) J Mech Phys Solids 53:1985
20. Cantournet S, Boyce MC, Tsou AH (2007) J Mech Phys Solids 55:1321
21. Sun C, Vaccaro E, Waite JH (2001) Biophys J 81:3590
22. Ogden RW (1984) Non-linear elastic deformations. Ellis Horwood, Chichester
23. Boyce MC, Arruda EM (2000) Rubber Chem Technol 73:504
24. Rief M, Gautel M, Oesterhelt F, Fernandez JM, Gaub HE (1997) Science 276:1109
25. Oberhauser AF, Marszalek PE, Erickson HP, Fernandez JM (1998) Nature 393:181
26. Fisher TE, Oberhauser AF, Carrion-Vazquez M, Marszalek PE, Fernandez JM (1999) TIBS 24:379
27. Smith BL, Schäffer TE, Viani M, Thompson JB, Frederick NA, Kindt J, Belcher A, Stucky GD, Morse DE, Hansma PK (1999) Nature 399:761
28. Kroner E (1960) Arch Ration Mech Anal 4:273
29. Lee EH (1969) ASME J Appl Mech 36:1
30. Odijk T (1995) Macromolecules 28:7016
31. Wang MD, Yin H, Landick R, Gelles J, Block SM (1997) Biophys J 72:1335
32. Qi HJ, Ortiz C, Boyce MC (2006) J Eng Mater Technol 128:509
33. Eyring H (1936) J Chem Phys 4:283
34. Bell GI (1978) Science 200:18
35. Minajeva A, Kulke M, Fernandez JM, Linke WA (2001) Biophys J 80:1442
36. Dorfmann A, Trimmer BA, Woods WA Jr (2006) J R Soc Interface (on line)
37. Mohandas N, Evans E (1994) Annu Rev Biophys Biomol Struct 23:787
38. Arslan M, Boyce MC (2006) J Appl Mech 73:536
39. Gosline JM, Guerette PA, Ortlepp CS, Savage KN (1999) J Exp Biol 202:3295
40. Qi HJ, Bruet BJF, Palmer JS, Ortiz C, Boyce MC (2005) In: Holzapfel GA, Ogden RW (eds) Mechanics of biological tissues. Proceedings IUTAM. Springer-Verlag, Graz, Austria, pp 180–205
41. Carrington E (2002) Limnol Oceanogr 47:1723
42. Moeser GM, Carrington E (2006) J Exp Biol 209:1996